Science and Technology for Energy Transition **77**, 17 (2022)

https://doi.org/10.2516/stet/2022015

Dossier LES4ECE'21: LES for Energy Conversion in Electric and Combustion Engines
Edited by Christian Angelberger, Stéphane Jay

Available online at:
stet-review.org

REGULAR ARTICLE OPEN ACCESS

CFD simulations of electric motor end ring cooling for improved thermal management

Ronald O. Grover Jr.[1,*], Xiaofeng Yang[1], Scott Parrish[1], Lorenzo Nocivelli[2], Katherine J. Asztalos[2], Sibendu Som[2], Yanheng Li[3], Cooper Burns[3], John Van Gilder[3], Nitesh Attal[3], and Oshin Avanessian[3]

[1] General Motors Company, 300 Renaissance Dr W, Detroit, MI 48265, USA
[2] Argonne National Laboratory, 9700 S Cass Ave, Lemont, IL 60439, USA
[3] Convergent Science Inc., 6400 Enterprise Ln, Madison, WI 53705, USA

Received: 8 December 2021 / Accepted: 16 May 2022

Abstract. Proper thermal management of an electric motor for vehicle applications extends its operating range. One cooling approach is to impinge Automatic Transmission Fluid (ATF) onto the rotor end ring. Increased ATF coverage correlates to enhanced heat transfer. Computational Fluid Dynamics (CFD) analytical tools provide a mechanism to assess motor thermal management prior to hardware fabrication. The complexity of the fluid flow (*e.g.*, jet atomization, interface tracking, wall impingement) and heat transfer makes these simulations challenging. Computational costs are high when solving these flows on high-speed rotating meshes. Typically, a Volume-of Fluid (VOF) technique (*i.e.*, two-fluid system) is used to resolve ATF dynamics within this rotating framework. Suitable numerical resolution of the relevant physics for thin films under strong inertial forces at high rotor speeds is computationally expensive, further increasing the run times. In this work, a numerical study of rotor-ring cooling by ATF is presented using a patent automated Cartesian cut-cell based method coupled with Automatic Mesh Refinement (AMR). This approach automatically creates the Cartesian mesh on-the-fly and can effectively handle complex rotating geometries by adaptively refining the mesh based on local gradients in the flow field which results in better resolution of the air-ATF interface. A Single non-inertial Reference Frame (SRF) approach is used to account for the rotating geometry and to further improve the overall computational efficiency. Quasi-steady state conditions are targeted in the analysis of the results. Important physics such as ATF jet structure, velocity detail near the air-jet interface, ATF coverage/accumulation on the ring surface, and cooling capacity are presented for a low-resolution Reynolds averaged Navier-Stokes (RANS), high-resolution RANS, and high-resolution Large-Eddy Simulation (LES) models. Computations are scaled over hundreds of cores on a supercomputer to maximize turnaround time. Each numerical approach is shown to capture the general trajectory of the oil jet prior to surface impingement. The high-resolution LES simulation, however, is superior in capturing small scale details and heat transfer between the free jet and surrounding air.

Keywords: Large Eddy Simulation, Electric motor, Computational Fluid Dynamics, Volume of Fluid Method, Adaptive Mesh Refinement.

1 Introduction

Even though automotive Original Equipment Manufacturers (OEMs) and suppliers have invested in novel combustion and aftertreatment strategies to reduce tailpipe and Greenhouse Gas (GHG) emissions of light-duty transportation vehicles [1–4], many of these advanced combustion and emissions strategies have not significantly proliferated into global vehicle fleets. Barriers include, but are not limited to, higher costs and complex control strategies when compared to vehicle fuel economy gains. Therefore, many OEMs are increasingly investing in alternative pathways and shifting away from traditional fossil fuel powertrains to electrified propulsion systems.

Battery Electric Vehicles (BEVs) offer the potential of an environmentally sustainable transportation infrastructure with zero tailpipe vehicle emissions. GHG reductions can be achieved if electricity is generated renewably (*e.g.*, solar, wind, thermal). In these vehicles, the Internal Combustion Engine (ICE) and fuel tank are replaced by an electric traction motor and battery. Electricity from the electrical grid is stored in the battery with lithium ion

* Corresponding author: ronald.grover@gm.com

Table 1. Comparison of magnet material properties [6].

	Ferrite	NdFeB	SmCo	AlNiCo
$(BH)_{max}$ (kJ/m^3)	10...35	200...400	150...230	35...60
T_{max} (°C)	225	150...230	250	450
αB_r (%/K)	−0.2	−0.15...−0.08	−0.06...−0.02	−0.03
αH_c (%/K)	0.2...0.5	−0.6...−0.4	−0.4...−0.2	0.2

being the most common for vehicle applications. The amount of stored electrical energy is proportional to the size and energy density of the battery pack. BEVs work synergistically with other automotive megatrends such as energy security, shared mobility, and autonomous vehicles.

BEVs have huge growth potential in the marketplace; however, several technical challenges exist that limit performance and increase cost. Improvements in energy density of lithium-ion battery packs have garnered considerable attention. Of equal importance is the durability and performance of the traction motor. Interior Permanent Magnetic (IPM) motors with NdFeB magnets are a common choice for BEVs due to their relatively high torque density, high Constant Power Speed Ratio (CPSR), and high efficiency [5]. The heat generation mechanism in electric traction motor includes (1) iron loss (or core loss) in the motor core such as hysteresis loss and eddy current loss; (2) copper loss in the winding due to Ohmic heating; (3) mechanics loss such as friction between shaft and bearing and windage loss due to the air drag. These generated heat during motor operation can cause considerable overheating on crucial components and poor thermal management degrades IPM performance. Irreversible demagnetization of the NdFeB magnets occurs if temperatures exceed material thresholds. Regulating the permanent magnet temperature is critical to IPMs. Table 1 shows a comparison of magnet material properties of four permanent magnets (Ferrite, NdFeB, SmCo and AlNiCo) with respect to magnetic strength, $(BH)_{max}$, maximum use temperature, T_{max}, temperature coefficient for remanent flux density, αB_R, and temperature coefficient for coercive field strength, αH_C [6]. Property ranges reported in the table span proportions of the constituent components of each magnet. NdFeB has the highest magnetic strength when compared to the other magnet materials, reinforcing its popularity for vehicle applications. On the other hand, NdFeB has the lowest maximum temperature limit making it vulnerable to demagnetization if not properly cooled.

For optimal performance, IPM magnets must be cooled within a proper temperature range to avoid irreversible damage [5]. In the marketplace, demagnetization limits the duty cycle of the motor and can limit performance. OEMs must use available toolsets to design proper thermal management systems to transport heat from the motor to the cooling fluid. The stator winding end-turns are a major source of heat generation and a significant contributor to copper losses. In practice, Automatic Transmission Fluid (ATF) is typically used as a coolant. Often ATF is both trickled over the winding end-turns of the stator and slung onto the end-turns from the rotor end cap. As motor designs are becoming more compact with high power density, proper cooling of the stator winding end-turns is increasingly more challenging [7].

Analytical toolsets are key enablers in the development of advanced thermal management systems for IPM motors. Proper motor cooling characterization involves quantifying the temperature of the stator winding end-turns, the coverage area of the ATF on the rotor end-cap, and the impingement of the ATF on the stator winding end-turns, which are crucial to accurately predict the winding end-turn cooling. For example, Figure 1 illustrates the stator winding end-turns and rotor end cap for a typical traction motor. A photo of a vehicle motor unit is shown on the left side of the figure, and the corresponding Computational Fluid Dynamics (CFD) predictions of the ATF film coverage on the rotor end cap is shown on the right. Quantifying the temperature and coolant coverage on the rotating rotor end cap is a challenge. Therefore, analytical toolsets relying on high-fidelity CFD simulations are becoming increasingly important. These tools can model coolant coverage on the end ring and predict heat transfer characteristics of prototype concepts prior to hardware fabrication; hence streamlining the design process. These simulations, however, are computationally intensive, requiring long runtimes due to large cell counts and small time steps to ensure accuracy.

In practice, product developers need to simulate coolant coverage at rotor speeds (*i.e.*, revolutions per minute, rpm) spanning two orders of magnitude (*e.g.*, 100 to 20,000 + rpm) over multiple rotor revolutions for "near steady" results. Computational meshes are typically 10–30 million cells and time steps can be less than 1 ms. For example, Srinivasan *et al.* [8] have simulated a rotor end cap for both the crown and weld sides of an electric motor using a VOF approach. To improve the liquid-air interface capturing, a predefined mesh is refined in the vicinity of the oil flow. The analysis is shown to capture the ATF coverage on the end ring for two rotor speeds. The study, however, is limited to a Reynolds averaged Navier-Stokes (RANS) k–e model to account for turbulence. The evolution of the initial jet and oil coverage is sensitive to the turbulence modelling approach [9]. In this study, we present a comparison of three numerical approaches (*e.g.*, "low-resolution" RANS, "high-resolution" RANS, and "high-resolution" Large-Eddy Simulation [LES]) to simulate the cooling of a motor end-cap by ATF. Each case utilizes an automated Cartesian cut-cell based method coupled with Automatic Mesh Refinement (AMR) to handle the complex rotating geometry by adaptively refining the mesh based on local gradients in the flow field to resolve the air-ATF interface. A Single non-inertial Reference Frame (SRF) setup is

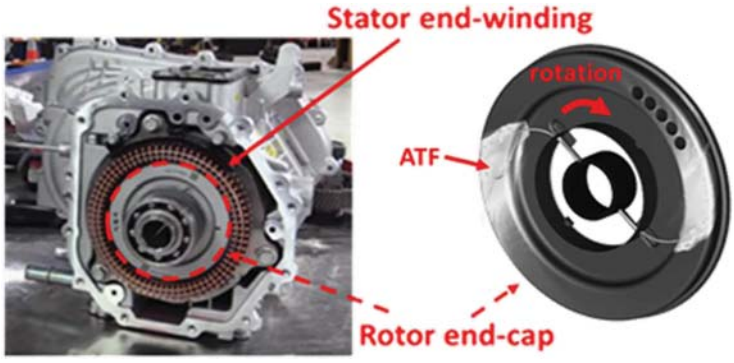

Fig. 1. Illustration of stator winding end-turns and rotor end cap for a typical traction motor.

used to account for the rotating geometry effect and to further improve the grid and overall computational efficiency. The low-resolution RANS simulation has a maximum of 3 million cells and is indicative of a common procedure to predict the liquid jet penetration at the fastest run time. The high-resolution RANS simulation has a maximum of 10 million cells to improve interface tracking which in turn leads to better ATF film coverage and heat transfer predictions. Finally, the high-resolution LES simulation has a maximum of 23 million cells for improved modelling of the initial jet breakup and subsequent wall impingement. All simulations are run to a quasi-steady state condition starting from a uniform quiescent condition. The high-resolution RANS/LES computations are initialized from a near steady low-resolution RANS flow field. Important physics such as ATF jet structure, velocity and vortex detail near the jet, and the ATF coverage/accumulation on the ring surface are reported.

2 Numerical model

The CONVERGE [10] code is used to solve a finite volume scheme based on the Cartesian cut-cell method originally proposed by Senecal *et al.* (2007) [11]. The governing momentum, energy, and turbulence transport equations are solved using a SIMPLE-like scheme on a collocated structured Cartesian cut-cell mesh. In this approach, the Cartesian cell is cut by the wall. In order to achieve good cell aspect ratio neighboring the wall, slender cells are merged with nearby full cells (cell pairing) based on a defined criterion. In this study a threshold of 0.3 was used, which means that if a cut-cell has a volume ratio of 0.3 to its neighbor cell, then these two cells will be merged. The cell pairing scheme is also found to improve numerical stability when used in conjunction with the good orthogonality of the interior Cartesian cells. Automatic variable time step control based on Courant–Friedrichs–Lewy (CFL) numbers is utilized. Message Passing Interface (MPI) and shared memory are used for a parallel run. Automatic Mesh Refinement (AMR) adaptively refines the mesh based on local sub-grid scale variations of velocity, temperature and void fraction (defined as gas volume fraction in the code) without foreknowledge of the evolving flow field [12]. Cells are only added when necessary, which reduces the overall simulation run time.

The first equation solved is the pressure/momentum correction/update. The solution algorithm is implemented within the main iteration loop until a specified convergence tolerance is satisfied. Then the temperature and turbulence transport equations are solved outside the main loop. To account for the multiphase flow physics, the Volume of Fluid (VOF) multiphase model (which is an Eulerian–Eulerian approach) is used for the ATF jet dynamics and heat transfer, with the gas volume fraction (or void fraction) α is defined as:

$$\alpha = \frac{\text{Volume of gas}}{\text{Volume of gas} + \text{Volume of liquid}}. \tag{1}$$

And the transport equation for void fraction is defined as:

$$\frac{\partial \alpha}{\partial t} + u \cdot \nabla \alpha = 0. \tag{2}$$

High Resolution Interface Capturing (HRIC) is utilized to blend upwind and downwind schemes for the convective term to balance resolution of the interface with numerical stability [13]. There are three steps to model the interfacial flux reconstruction. For the first step, the flux constructing scheme continuously monitors first order upwinding, first order downwinding, and second order upwinding based on the normalized cell face scalar values. Next, the angle between the interface normal directions relative to the cell normal direction is computed for each scheme. Upwind differencing is applied to the largest angles to avoid unphysical alignment of the interface with the mesh. A blending factor is used to smoothly transition between the downwind and upwind schemes. Here, more first order upwinding leads to better stability. Finally, a time step defined by the convective CFL number is determined. In this work, the max convective CFL number is set to be 0.5. To avoid the common checker-boarding issue for collocated cells, the scheme from Rhie and Chow [14] is used for pressure-velocity coupling.

RANS and LES approaches are applied to model turbulence effects. RANS approaches often provide a decent balance between numerical stability and low computational cost. This study uses the Shear Stress Transport (SST-k-Omega) RANS model [15]. The transport equations

Fig. 2. Geometry of the rotor end ring.

are solved by Successive Over-Relaxation (SOR) algorithm. At the wall boundary, enhanced law-of-the-wall models are used for the velocity/temperature solution for the first layer of cells. For the LES computations, a zero-equation dynamic Smagorinsky model [16] is used with the Wenger–Werner wall model for the near wall treatment when y^+ is greater than 1. Standard model constants are used for all computations.

3 Computational setup

The geometry studied is a rotor end ring from a full-sized electric motor shown in Figure 2. The ATF oil enters *via* two drilled holes through the rotor shaft. The oil enters the shaft at a temperature of 363 K, is slung from two holes into the end ring region, and subsequently impinges on the ring surfaces. The end ring is directly exposed to the ambient air environment. The geometry is rotating at a constant speed of 8000 rpm. Both the gas and liquid phases are treated as incompressible. The constant liquid properties are as follows: density of 793 kg/m^3, thermal conductivity of 0.139 W/m K, specific heat of 2037 J/Kg K, and viscosity of 5.83e-3 Pa s. The gas phase (air) density is 0.91 kg/m^3 based on a reference pressure of 1 atm and temperature of 380 K.

For the inlet boundary condition, the ATF inflow is specified with a constant mass flow of 0.017 kg/s at 363 K which corresponds to 1.56 m/s of mean velocity for each nozzle (defined as the superficial velocity of the AFT in the pipe). The outflow boundary is connected to the ambient. It is prescribed with a constant pressure of 1 atm and zero normal gradient for backflow. The conjugate heat transfer between the solid and the fluid is not considered. The inner walls of the domain (shaft) have a specified wall temperature of 363 K which is the "cold" oil temperature at injection. The outer walls (nozzle and ring) have a wall temperature of 423 K (highest temperature in the domain), which is representative of a warmed-up operating condition. A Single non-inertial Reference Frame (SRF) is used to model the full domain. All wall boundaries rotate at the same speed.

Simulations are carried out on the Theta supercomputer using CONVERGE version 3.0. The LES results are compared to more affordable RANS simulations to highlight the influence of grid resolution and numerical approach on ATF surface coverage and resulting heat flux. Representative mesh topologies and numbers are shown in Figure 3 and Table 2. For the high-resolution LES computations, the base cell size is 1.5 mm and the minimum grid is smaller than 0.1 mm resulting in a total cell count is 23 million. The liquid–gas interface for the outer domain is refined using AMR based on the curvature of the void fraction field, which the inner domain (shaft and nozzle) is refined with fixed, highest level of refinement. The high-resolution RANS simulation has the same base and minimum cell sizes as the LES computations but using a higher AMR threshold that reduces the total cell count to 10 million. The low-resolution RANS case has higher minimum and base cell sizes compared to the high-resolution simulations limiting the total cell count to 3 million.

4 Results

4.1 Mesh resolution study

An accurate solution for the jet/film dynamics and heat transfer is heavily dependent on the underlying mesh to resolve the initial jet disintegration, droplet breakup, and eventual ATF impingement on the ring surface. Additionally, a sufficiently fine resolution is required for LES to reduce the sub-grid scale error and to improve the accuracy of near wall predictions. A grid sensitivity study is necessary to verify the chosen LES grid resolution minimizes numerical errors that will confound physical understanding.

A simplified "half" end cap rotor geometry (180 degrees with respect to one nozzle) was used to study the mesh resolution effect for the high-resolution LES setup at reduced computational expense. The weight balancing holes were neglected in the model setup. The same grid control strategy in Figure 3c is used for consistency. The minimum cell size ranges between 20 μm and 220 μm with corresponding y^+ values spanning from 1.5 to 11. The ring surface film temperatures for the various grid resolutions are shown in Figure 4. An approximate grid-independent solution is achieved with a minimum resolution less than 70 μm. This mesh resolution projects to 50 million cells for the full geometry leading to a greater than 2× increase in computational cost over the setup highlighted in Figure 3c. Therefore, a minimum grid size of 93 μm is chosen as an optimal balance between accuracy and numerical error. The selected grid has a 2 K discrepancy in temperature when compared to the grid converged solution. Further, the initial jet structure is well-captured by the 93 μm cell size.

4.2 Scalability study

Due to the large cell counts required to resolve the ATF coverage, a scalability study is performed to assess the range of potential wall times given limited computational resources. An analysis is performed for each computational approach run over different Crank Angle Duration (CAD): low-resolution RANS setup (~2.6 million cells peak count is achieved), high-resolution RANS (~8.4 million cells), and high-resolution LES setup (~20.2 million cells). The purpose of these speed-up tests is to determine the optimal code scalability to manage compute resources necessary to enable the exploration of high-fidelity simulations.

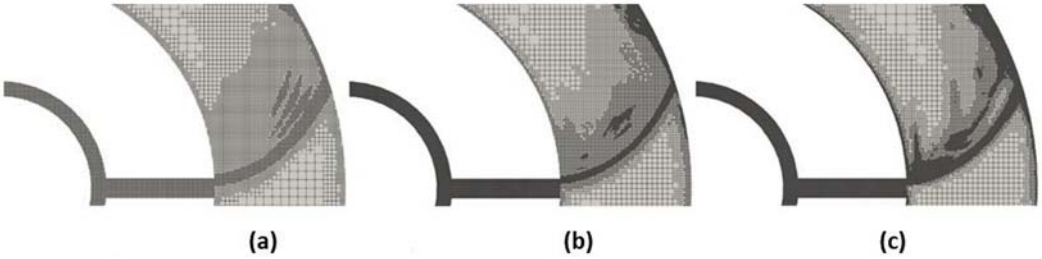

Fig. 3. Overview of the numerical grid for (a) low-resolution RANS, (b) high-resolution RANS, and (c) high-resolution LES model.

Table 2. Summary of the grid for low-resolution RANS, high-resolution RANS and high-resolution LES model.

	Low-resolution RANS	High-resolution RANS	High-resolution LES
Base cell size (mm)	2.5	1.5	1.5
Minimum cell size (μm)	156	93	93
Total cell count (million)	3	10	23

The software performance tests have been conducted at quasi-steady conditions by operating the code for a wall-time of 10 h.

4.2.1 RANS scalability results

Scalability tests were performed for the low- and high-resolution RANS setups using the Intel Broadwell compute nodes. The low-resolution RANS simulation setup is the smallest numerical simulation presented here, with approximately 2.6 million cells and a linear speed-up is measured up to 324 CPUs, which can be seen in Figure 5a. Figure 5b shows an optimal distribution of the computational cells on the CPUs at ~10 k cells/CPU for this allocation, which balances the memory usage and communication cost. Figure 5c shows even load balancing of cells across all compute cores.

The performance of the code for the high-resolution RANS – with 8.6 million cells at quasi-steady state – is reported in Figure 6a. Extremely good speed-up is measured up to 720 CPUs for the high-resolution RANS case as shown in Figure 6b. The distribution of the cells per CPU is again key, as shown in Figure 6c, where a limit of 10 k cells/CPU is reached for the largest tested allocation. Therefore, it can be concluded that for larger allocations and larger cell counts maintaining a uniform distribution of cells yields an efficient speed-up. This represents a helpful guideline for more computationally complex simulations that are of interest in refining and capturing the relevant physics.

4.2.2 LES scalability results

To optimize the computational resources available for the project, the simulations of the large high-resolution LES test case have been performed on both Broadwell and Knights Landing (KNL) compute nodes. Because of their different architecture, the two systems show different wall times, but the code reports comparable speedup performance. As highlighted for smaller CFD setups, the code behaves efficiently when the number of cells/CPU is maintained above ~10 k cells/CPU per case, as shown in Figure 7c. Table 3 reports a summary of the code runtime performance assessment for the three tested cases.

4.3 Pre-impingement jet dynamics

Prior to ATF impingement on the motor end-ring, the effect of modelling approach on the initial jet structure is studied. Although the bulk jet trajectory is found to be similar for each numerical approach, there are subtle differences on the liquid–gas interface that affect the subsequent wall film (Fig. 8). Here we choose the isosurface criteria of liquid volume fraction = 0.05 based on two reasons, firstly to better illustrate the detailed splash far away from the impinge location; and secondly in the CONVERGE code, the local cell thermal properties (thermal conductivity, heat capacity) of VOF simulation are averaged by mass fraction, hence the liquid void fraction of 0.05 is equivalent to a liquid mass fraction of 0.87, which still dominates the local heat transfer. The high grid resolution RANS and LES cases capture fractions of liquid entrained by the gaseous cross flow along the jet path toward the wall. These secondary streams of liquid generate a larger initial impingement footprint, which is visible in Figures 8b and 8c. Moreover, LES near wall velocity treatment, coupled with the higher grid resolution, results in a stronger dissipation of the jet tangential momentum on the wall, which will be further analysed in the manuscript.

The columnated jets for each simulation have been analyzed through cross-sections taken at various locations in the stream wise direction spanning internal to the nozzle to near the location of impact with the wall. Figure 9 shows an ATF jet through the jet center-plane location. The labelled stream-wise locations are as follows: r_1 at the feeding

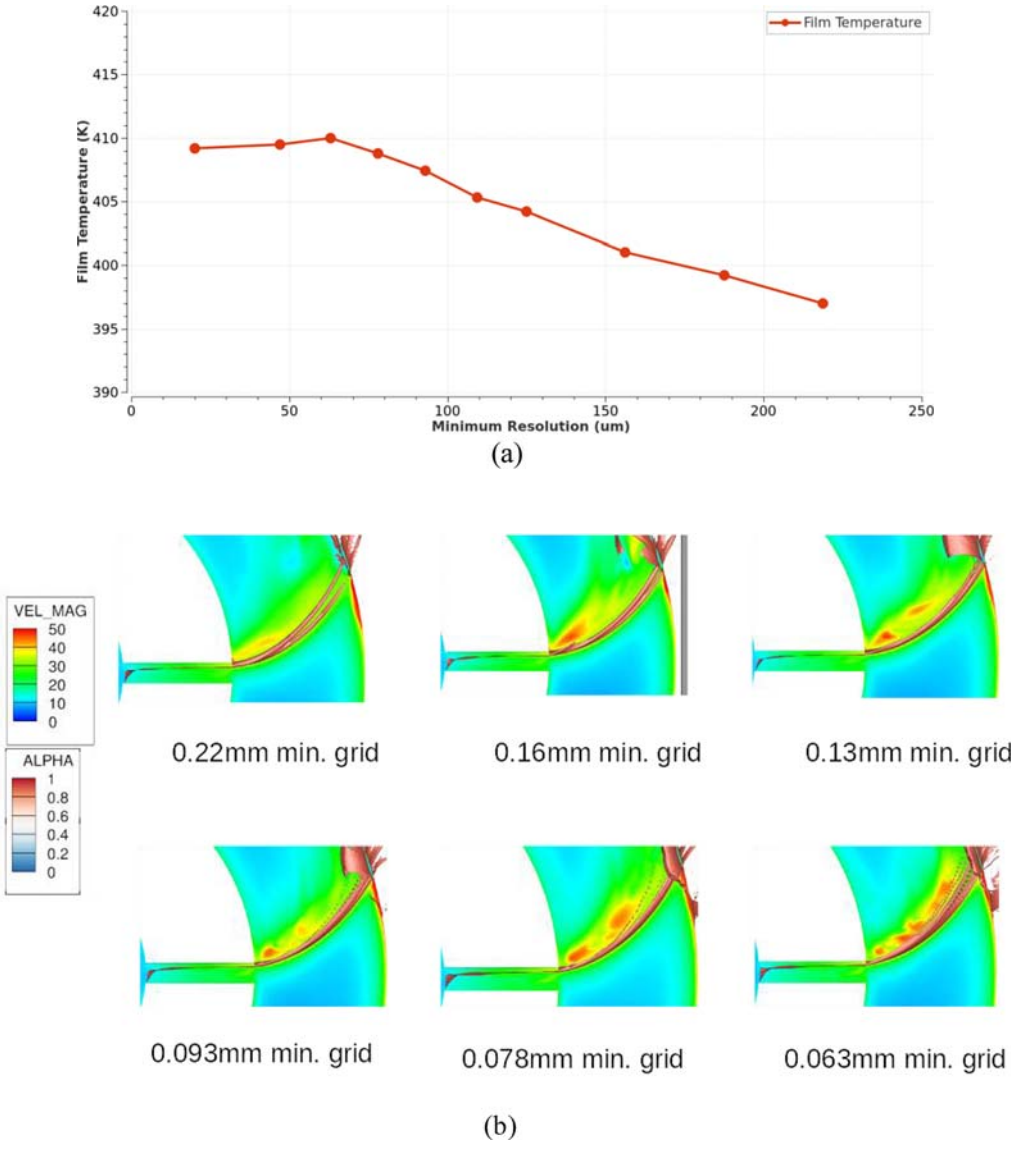

Fig. 4. Sensitivity of (a) film temperature and (b) initial jet dynamics to computational mesh size. The film temperature is less mesh dependent at cell sizes smaller than 70 μm. The initial jet structure is plotted as a velocity contour and isosurface of void fraction equal to 0.9.

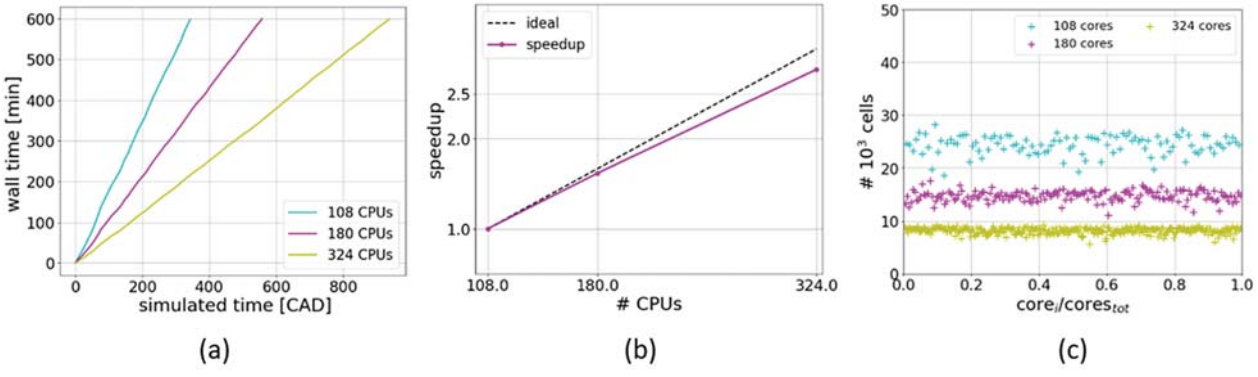

Fig. 5. Results for low-resolution RANS scalability tests (a) wall time comparison (b) speedup (c) cell distribution per core.

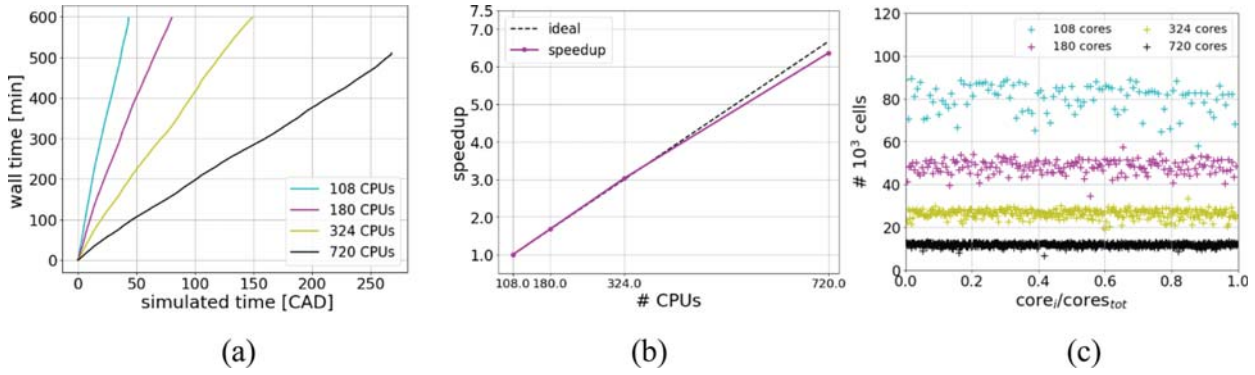

Fig. 6. Results for high-resolution RANS scalability tests (a) Computational cost at different allocations, (b) speedup, and (c) cell distribution per core.

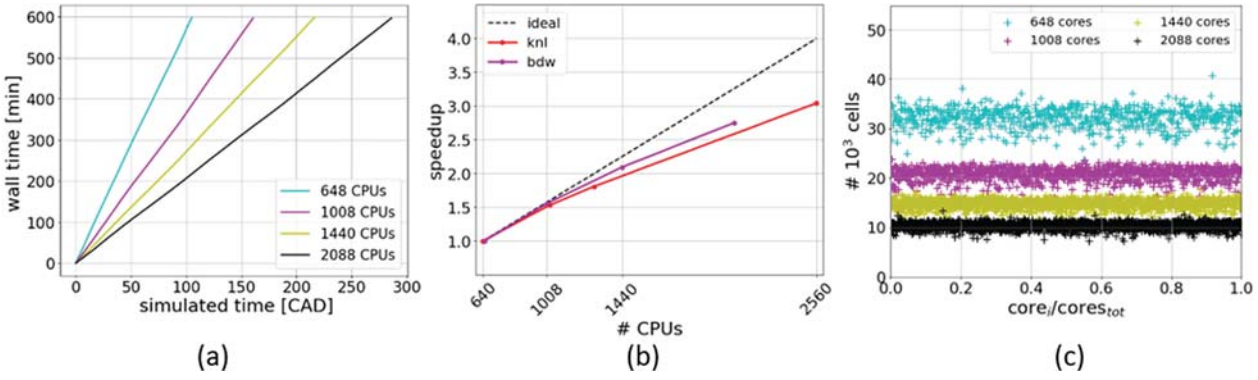

Fig. 7. Results for high-resolution LES scalability tests: (a) simulated time per number of CPUs for Broadwell nodes, (b) ideal versus actual speedup for both Broadwell and KNL nodes, and (c) cell distribution per core.

Table 3. Summary of the code performance assessment for three tested cases.

Label (estimate)	Base mesh	# CPUs	Wall time (hrs)	Total cell count (millions)	Wall time [hrs]/ rotation
Low-resolution RANS	2.5 mm	108	10	~2.60	10.5
		180			6.4
		324			3.8
High-resolution RANS	1.5 mm	108	10	~8.60	83.3
		180	10		44.7
		324	10		24.1
		720	8		10.8
High-resolution LES	1.5 mm	648	10	~20.2	34.2
		1008			22.4
		1440			16.6
		1280 (KNL)			58.5
		2088			12.6
		2560 (KNL)			34.4

pipe exit or 0.031 m from rotating center, r_2 a plane at 0.04 m from the rotating center, and r_3 at 0.047 mn from the shaft center, a location of the jet prior to the impingement on the rotor surface.

As can be observed in Figure 10a, the interface between liquid and gas is strongly diffused in the low-resolution RANS case, especially when compared to finer resolution cases shown in Figures 10b and 10c. As the jet advances

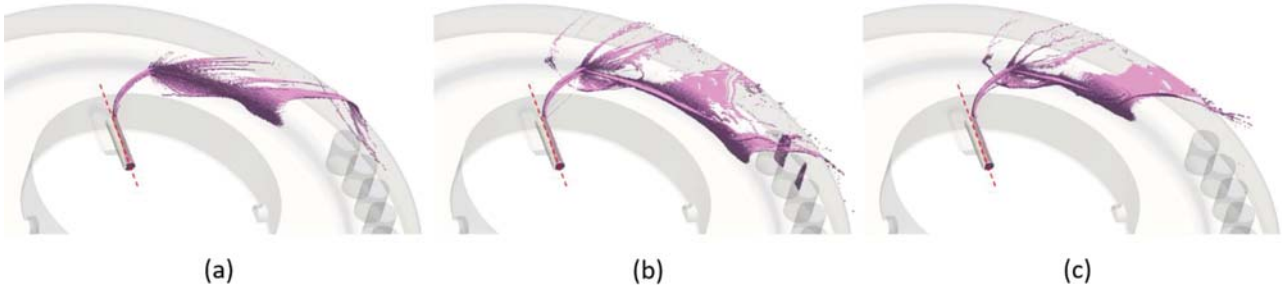

Fig. 8. Iso-surface of liquid volume fraction = 0.05 showing the initial jet structure and impingement for the (a) low-resolution RANS, (b) high-resolution RANS, and (c) high-resolution LES simulation cases.

Fig. 9. stream-wise locations selected for ATF jet analysis on iso-volume of void fraction = 0.95 from the high-resolution LES simulation.

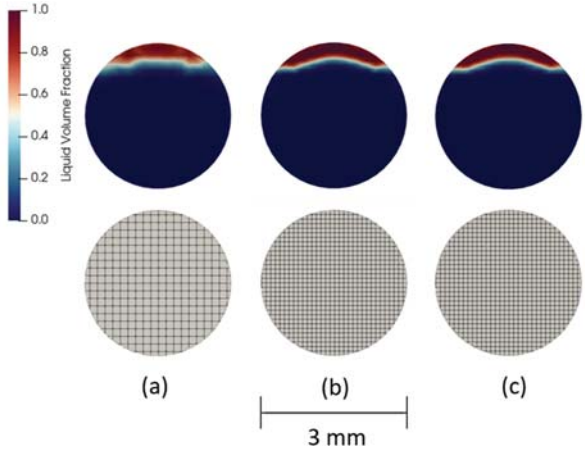

Fig. 10. cross-sections of the jet located at the nozzle exit r_1, contoured by liquid volume fraction, for (a) low-resolution RANS, (b) high-resolution RANS, and (c) high-resolution LES.

in the stream wise direction and exits the nozzle, the higher numerical diffusion provided by the low-resolution RANS case results in a wider primary jet footprint than the high-resolution RANS and LES cases.

Enhanced diffusion and mixing cause a blurry interface of the jet for the low-resolution RANS case (see Fig. 11a), as well as a larger spatial dispersion of void fraction when compared to the high-resolution RANS case shown in Figure 11b, and high-resolution LES case, shown in Figure 11c. However, the overall shape of the jet is consistent for the three simulations studied, with the main difference being the development in a sharper interface as the resolution increases.

As the jet continues to transverse in the streamwise direction, the effect of greater numerical diffusion in the coarse grid computation amplifies. The pattern of higher diffusion and enhanced mixing is observed in the low-resolution RANS case, as can be seen in Figure 12a, where the interface continues to be blurry and the void fraction lower than that for the higher-resolution computational cases. The high-resolution RANS case (shown in Fig. 12b) exhibits a similar shape to the jet captured in the low-resolution RANS setup, but with a clearly defined interface, indicating a more intact jet structure.

Figure 12c shows the high-resolution LES case with more prominent breakup compared to the high-resolution RANS case when approaching the wall, although the overall "C" shape of the cross-section is consistent with the two RANS setups. Furthermore, the radial jet velocity magnitude, velocity angle, and jet position averaged over the jet stream-wise cross-sectional area shows that these three approaches have comparable bulk jet dynamics (Fig. 13). For the velocity plot (Fig. 13a), the magnitude is averaged by the mean liquid supply velocity at the nozzle inlet, which is 1.6 m/s. The D_c here is a reference diameter of 0.063 m and $r/D_c = 0$ is at nozzle entrance, $r/D_c = 0.25$ is at nozzle exit and the impinge location is at $r/D_c = 0.51$.

The global structure of the oil jet is sensitive to its initial atomization. It is important to model this process accurately to achieve representative downstream predictions. In lieu of available experimental measurements for the simulated condition, the computed jet structure is compared to a canonical spray in crossflow configuration where breakup regime maps have been extensively characterized in the literature. The atomization regime and images of the jet structure (isosurface of $\alpha = 0.9$) for the low-resolution RANS, high-resolution RANS and high-resolution LES cases are shown in Figure 14. The regime map is plotted as a function of Jet Reynolds number ($\mathrm{Re_L} = \rho_L V_{jet} d/\mu \sim 4000$, where ρ_L is liquid density, V_{jet} is liquid radial velocity at nozzle exit, d is the nozzle diameter and μ is the liquid viscosity) and Weber number ($\mathrm{We} = \rho_{air} U^2_{air} d/\sigma \sim 32$, where ρ_{air} is air

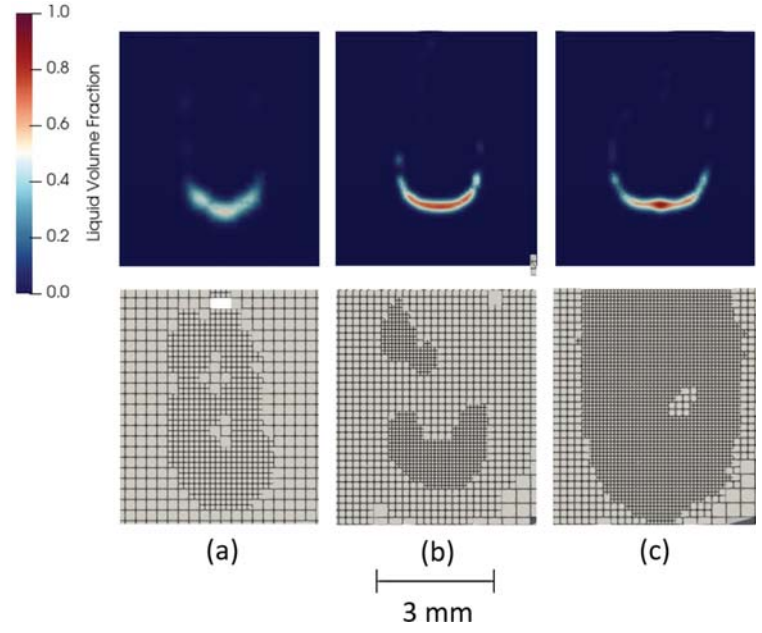

Fig. 11. cross-sections of the jet located at $r_{2,}$ contoured by void fraction, for (a) low-resolution RANS, (b) high-resolution RANS, and (c) high-resolution LES.

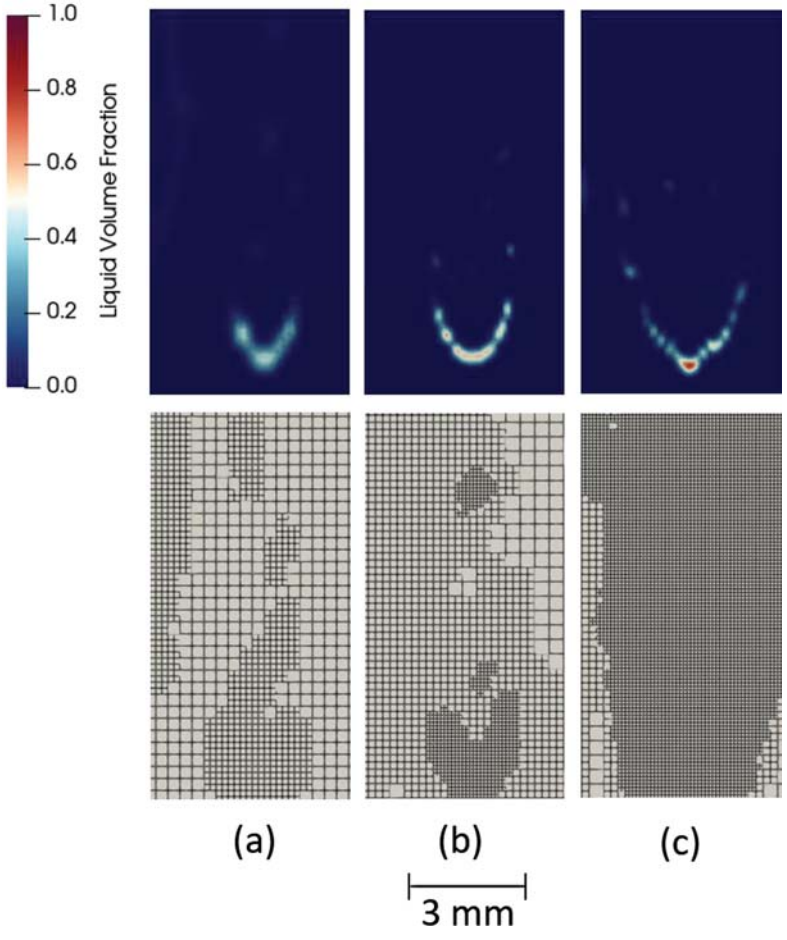

Fig. 12. cross-sections of the jet located at r_3, contoured by void fraction, for (a) low-resolution RANS, (b) high-resolution RANS, and (c) high-resolution LES.

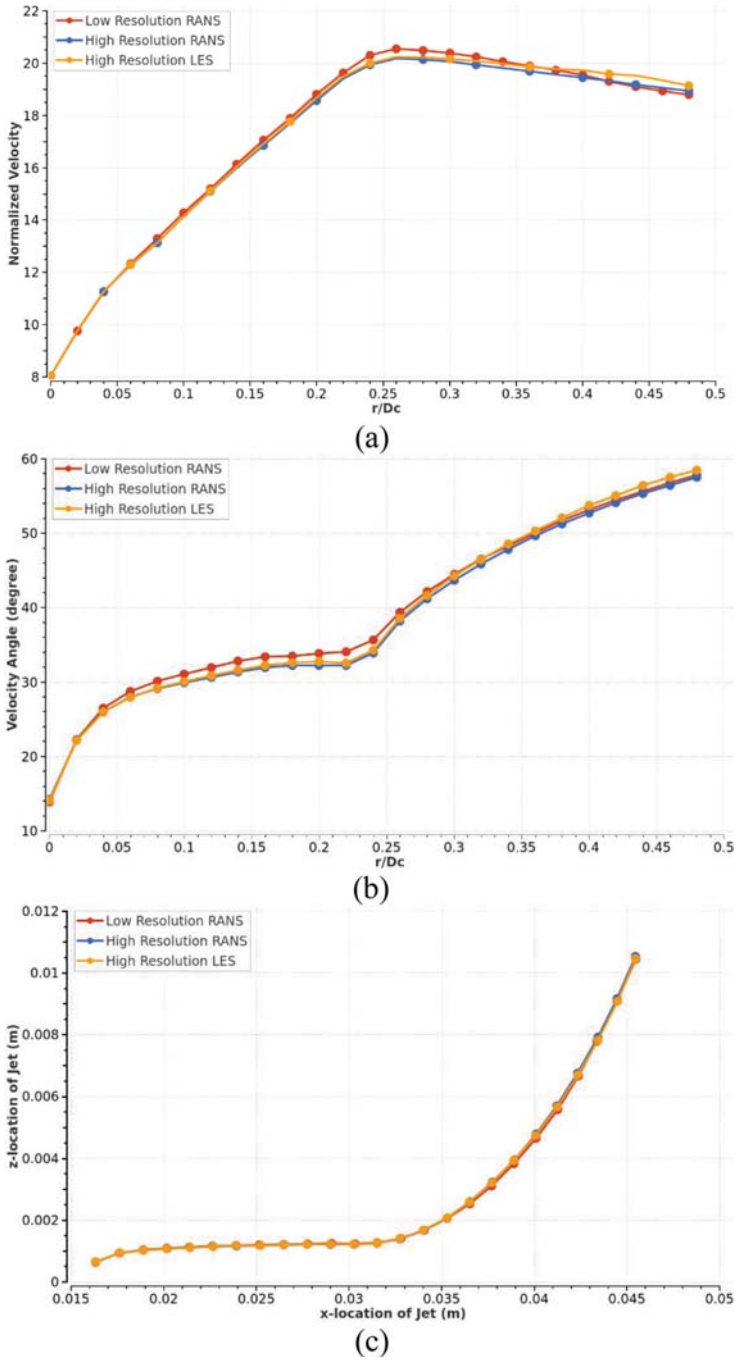

Fig. 13. Radial distribution of (a) Jet velocity magnitude (b) Jet velocity angle (c) Jet z-location.

density, U^2_{air} is air velocity at nozzle exit, d is the nozzle diameter and σ is the liquid surface tension) following the recommendation of [17]. The plot subdivides the column breakup regime, where the fluid remains an intact core prior to downstream disintegration, and the surface breakup regime, where superficial breakup occurs shortly after the nozzle exit. The current jet is characterized in the column breakup regime. The atomization behaviour is noticeably borderline to surface breakup due to the bias in the jet flow exiting the nozzle (see Fig. 8). Since the liquid does not fill the entire nozzle cross sectional area, the exit velocity is significantly larger than the prescribed inlet boundary condition of 1.6 m/s (see Fig. 13a). A similar internal nozzle flow has been visualized and reported [18]. The overall jet trajectory (velocity angle and spatial location) from all three approaches predicts a similar column break up regime. The high-resolution LES model computes more prominent breakup due to the shear driven Kelvin–Helmholtz instability along with rotational acceleration initiating Rayleigh–Taylor instability [19–22].

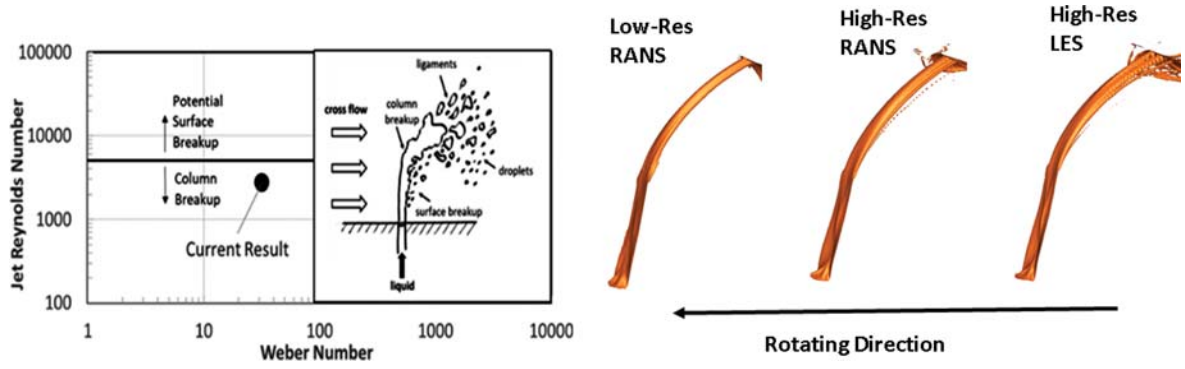

Fig. 14. Jet contour comparison for three studied models.

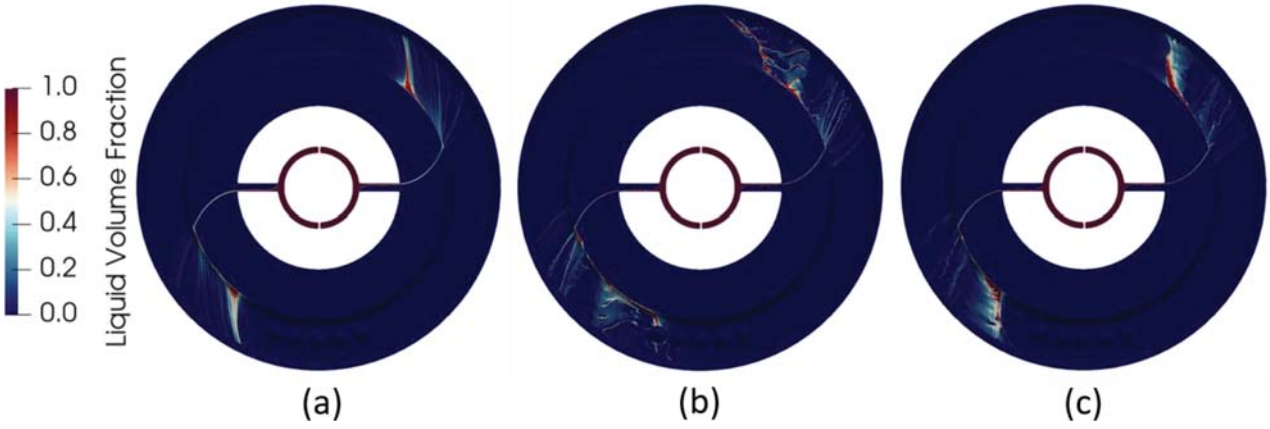

Fig. 15. Void fraction profiles along the jet path to the impingement surface at quasi-steady state conditions for (a) low-resolution RANS, (b) high-resolution RANS, and (c) high-resolution LES.

4.4 Jet impingement and splash dynamics

A pivotal parameter in the assessment of the cooling potential is the surface liquid coverage. Given the high heat transfer coefficient of the impinging fluid, the cooling potential strictly correlates with the liquid film area, which needs to be maximized in the system design process. The three proposed numerical approaches predict different impingement footprints on the rotating walls. Figure 15 reports the void fraction along the centerline of the jet to the rotor wall. It clearly shows that with higher mesh resolution in the RANS setup – Figures 15a and 15b – the liquid impact generates finer splashing structures, enhancing the cumulative coverage on the surface. Compared to the low-resolution RANS setup, the high-resolution RANS and LES setups have more ATF accumulation ahead of the impingement location along the rotating direction. High-resolution LES setup shows wider dispersed oil film pattern while the high-resolution RANS model shows more segregated oil streaks, which is mostly related with the velocity field of the film on the surface that will be discussed later in Figure 17.

The trends in surface liquid coverage, defined as the total area of the surface faces covered by liquid, are reported in Figure 16. It is evident that the high-resolution RANS and LES setups predict higher coverage than that of a low-resolution RANS result, while the velocity and turbulence fields near the ring surface predicted by high-resolution RANS allow more film accumulation compared to that of the high-resolution LES setup. It is possible to notice that the high-resolution cases start from a quasi-steady state solution instead of start from fresh cold condition, to save computation time. Since the domain has been initialized with the results from the low-resolution RANS case, the CPU-cost of the jet/film development transient can be largely reduced. And due to larger resolved flow fluctuation at finer resolution, it takes longer time for the high-resolution cases to stabilize, while the numerical diffusion for the low-resolution RANS case stabilized the flow sooner.

The higher spreading of the liquid on the rotor end-ring surface predicted by the high-resolution LES case results in a larger cooling footprint. In Figure 17, the motion of the liquid jet, isolated as the portion of the domain with void fraction lower than 0.95, is represented by its relative velocity to the solid wall rotation (defined as the absolute liquid velocity in the first layer of cell near the ring surface, minus the corresponding local wall velocity). Higher grid resolution generates slower film spreading on the external walls of the rotor end ring, which will be instrumental for the prediction of the film stripping and re-atomization

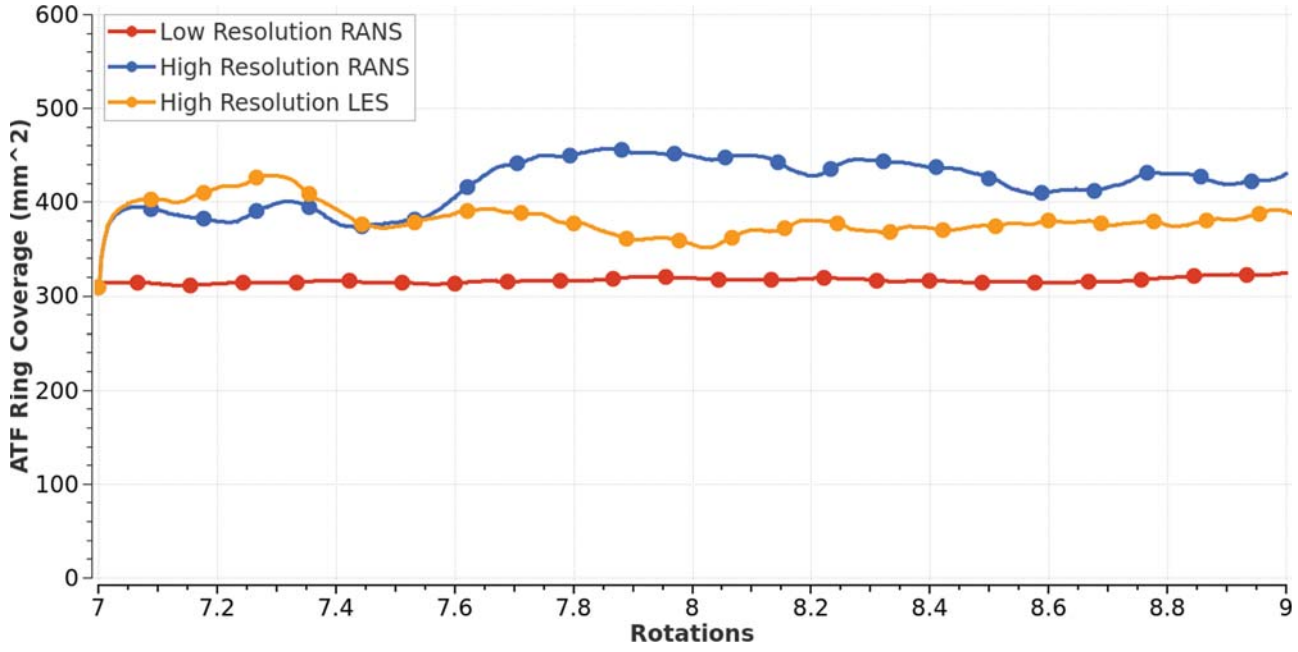

Fig. 16. Surface coverage trends for the three tested simulation setups.

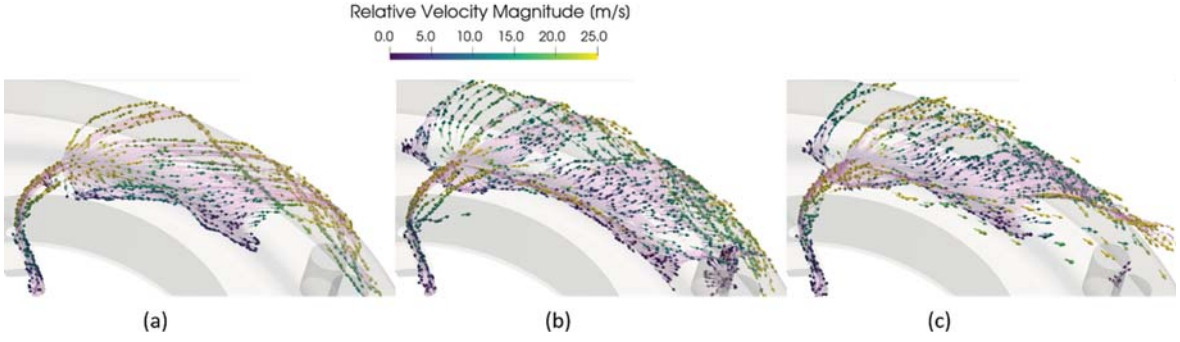

Fig. 17. Relative velocity between the liquid jet and the surface rotation for: (a) low-resolution RANS, (b) high-resolution RANS and (c) high-resolution LES.

directed towards the stator end windings (not shown). Moreover, the high-resolution RANS predicts the largest dispersion of the film momentum, which contributes to the wavy film pattern as shown in Figure 15 and allows slightly higher coverage of the surface and slower centrifugal motion of the liquid on the walls compared with the high-resolution LES results.

4.5 Heat transfer analysis

The effect of numerical approach on the heat transfer between the liquid jet and surrounding air along with the liquid jet-wall interaction is studied. The temperature of the jet is analysed at the same transverse locations reported in Figure 9 at quasi-steady operation. The cross-section of the jet at the exit of the feeding pipe can be examined in Figure 18, where the low-resolution RANS case (Fig. 18a) shows less warming of the bulk jet compared with the high-resolution RANS case (shown in Fig. 18b). The LES simulation (Fig. 18c) shows the highest heat-up of the liquid jet in the feeding pipe, which is mainly due to the difference in the predicted turbulence between RANS and LES and the near wall treatment in the nozzle considering a $y^+ \sim 5$.

When interacting with the air cross-flow, the jet temperature profile retains a more distinct "C" shape for the high-resolution LES case (Fig. 19c) as compared with the low-resolution RANS case (Fig. 19a). The higher numerical diffusion coupled with the isotropic turbulence assumption of low-resolution RANS generates more thermal diffusion between phases. The high-resolution RANS case shows results in between that of the other two setups.

Finally, as the jet continues in the stream-wise direction, the predicted temperature for all three numerical approaches is similar to the ambient air temperature due

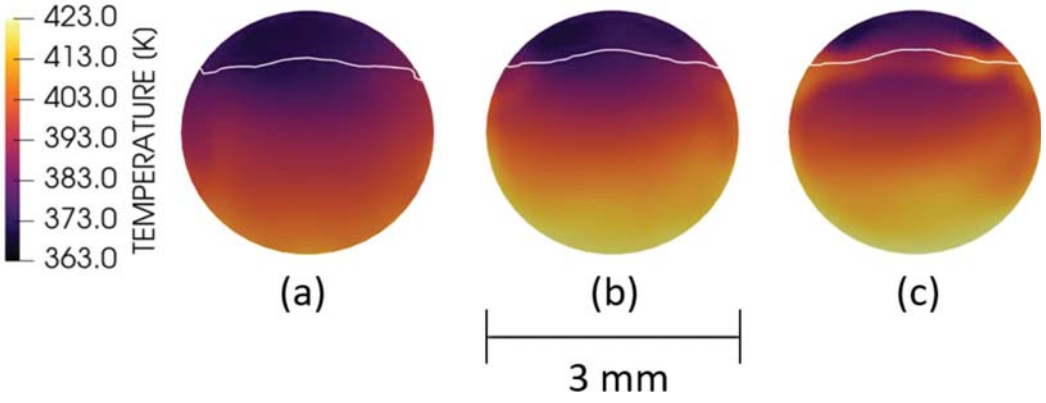

Fig. 18. cross-sections of the jet located at the nozzle exit r_1, contoured by temperature, for (a) low-resolution RANS, (b) high-resolution RANS, and (c) high-resolution LES.

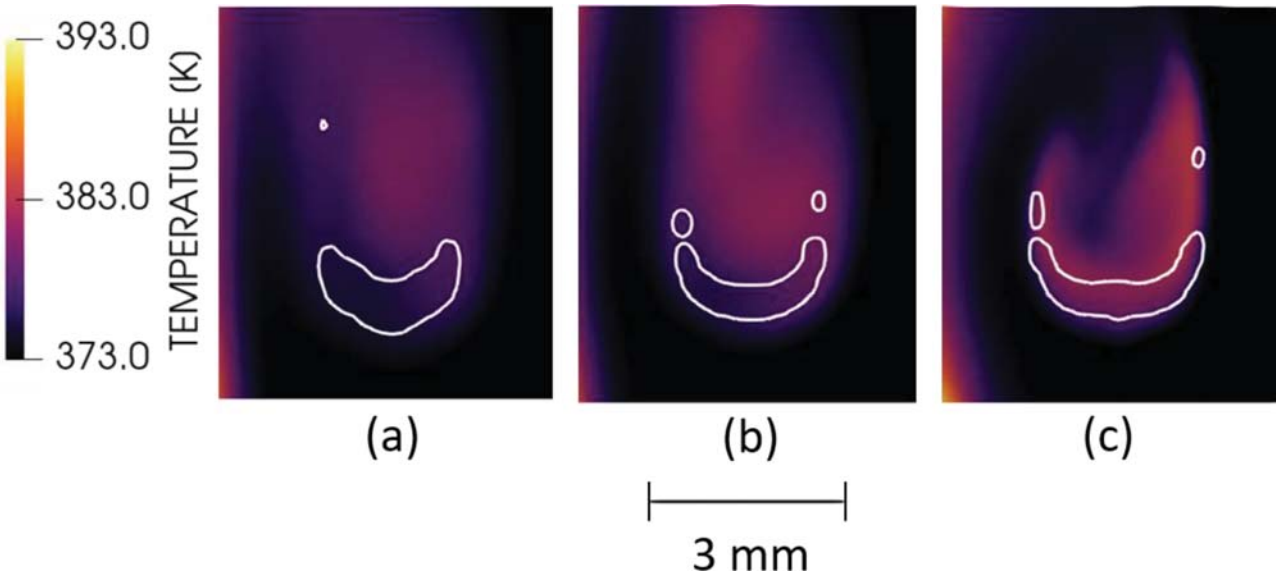

Fig. 19. cross-sections of the jet located at r_2, contoured by temperature, for (a) low-resolution RANS, (b) high-resolution RANS, and (c) high-resolution LES.

to sufficient time for heat transfer (Fig. 20). Upon impingement, the high-resolution LES shows the least thermal diffusion at the liquid–air interface. Overall, turbulence isotropy has a strong effect on the jet development in cross flow. The thermal evolution of the jet towards the impingement surface highlights this behavior, illustrating how the lower density regions in the vicinity of the jet, representative of a more diffused liquid phase, are significantly cooler for the RANS, especially for lower grid resolutions.

The temperature of the liquid jet near the impingement location is an indicator of the energy potential available to transfer from the wall to the ATF. The current numerical framework assumes a prescribed constant wall temperature. Nevertheless, the thermal transient of the liquid film is an indication of the maximum heat transfer achievable. By integrating the film temperature (first layer of cell's temperature) on the ring surface, we can get the volume-averaged near-wall temperature of 402.2 K for the low-resolution RANS setup, 407.1 K for high-resolution RANS setup and 408.8 K for high-resolution LES setup, as shown in Figure 21. The LES result shows elevated non-wetted surface temperature at the current resolution of $y^+ \sim 5$. Figure 22 shows the comparison of the jet streamwise temperature profile averaged over the jet cross-sectional area for each numerical approach. Although each case predicts similar bulk jet temperature upon impingement, the high-resolution LES setup shows faster heat-up of the jet after exiting the nozzle (which is illustrated in Fig. 18) but cooled down by the surrounding cool air before impingement. The results highlight a key difference between LES and RANS turbulence models. The LES formation is less diffusive resulting in a larger downstream liquid-gas surface area for heat transfer produced by

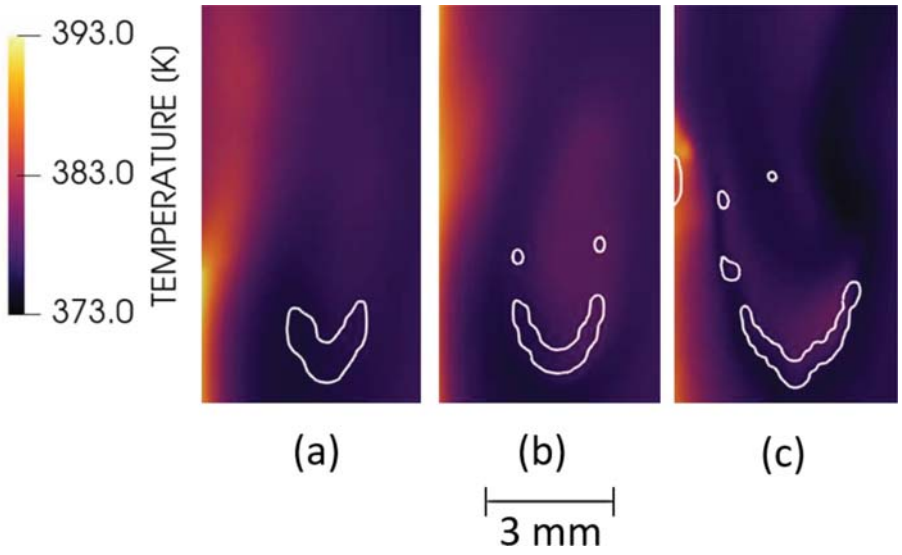

Fig. 20. cross-sections of the jet located at r_3, contoured by temperature, for (a) low-resolution RANS, (b) high-resolution RANS, and (c) high-resolution LES.

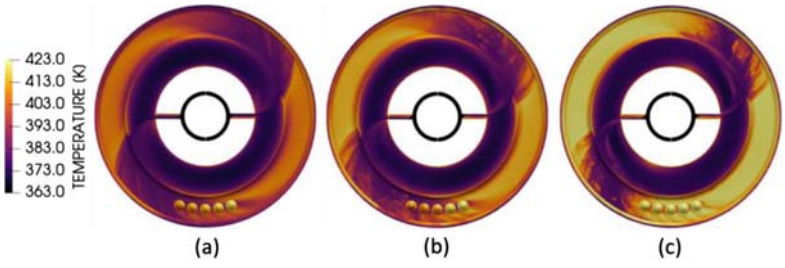

Fig. 21. Temperature profiles along the jet path to the impingement surface at quasi-steady state conditions for: (a) low-resolution RANS, (b) high-resolution RANS, and (c) high-resolution LES.

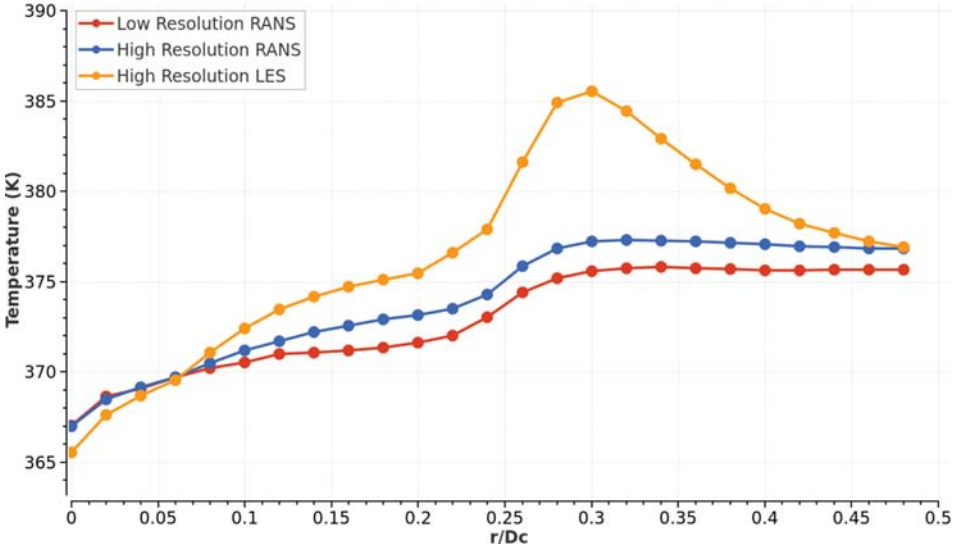

Fig. 22. Radial distribution of jet temperature for three studied models.

structures in the flow rather than turbulence viscosity in RANS models smearing these features.

5 Conclusion

A VOF approached applied to an underlying automatic Cartesian cut-cell based approach with AMR is adopted to model the ATF cooling of a rotor end-ring of an electric motor. Three turbulence models are studied at different mesh resolutions: low-resolution RANS, high-resolution RANS, and high-resolution LES. Low-resolution RANS can capture the basic dynamics of the jet at the lowest computational cost of the cases simulated. However, it suffers to properly model the liquid-air interface of the ATF jet leading to an under-prediction of oil coverage on the end ring surface. High-resolution RANS does better in predicting the jet structures and film formation compared to low-resolution RANS. The trade-off is higher computational expense. Finally, high-resolution LES does the best in resolving small scale structures and film development on the ring surface. The LES predictions are noticeably different than both RANS formulations when comparing jet dynamics and heat transfer in totality. The trade-off is significantly higher computational expense. Therefore, super computing resources are utilized to optimize scalability and computational efficiency.

The scalability of the numerical code is leveraged to improve turnaround time. The software shows good performance for the three different cases. The cell distribution on the CPUs is found to be optimal at 10 k cells per core. The solver exhibited greater than 70% speedup to 2000 + cores for the high-resolution LES computation, with the core count of 648 from baseline run (speedup = 1).

Each numerical approach generally predicts similar overall jet dynamics (*i.e.*, bending angle and velocity profile along the jet). The LES simulation shows more prominent breakup due to better resolution of shear-driven Kelvin–Helmholtz and centrifugally-driven Rayleigh–Taylor instabilities. The thermal profiles show RANS solutions are overall more thermally diffusive due to higher numerical diffusion and turbulence viscosity. Eventually, all modelling approaches show similar jet temperature once they impinge on the rotor wall despite different predicted temperatures upon exiting the nozzle. The faster heat-up of the jet at the nozzle exit for high-resolution LES setup is mainly due to less numerical diffusion at the liquid–air interface along with a near wall model valid for $y^+ \sim 5$. Farther downstream after the jet impinges on the end ring surface, the resulting heat transfer with the wall is closely related to the liquid coverage on the ring surface. The high-resolution RANS or LES setup exhibits a larger ATF coverage area compared to low-resolution RANS.

Future work includes simulating a moving geometry with and inlaid boundary layer mesh to better capture the near wall behavior of the jet splash. Additionally, an Eulerian–Lagrangian Spray Atomization (ELSA) model is being developed to better capture the breakup of the initial jet by coupling the Eulerian–Eulerian model (VOF) within the nozzle to an Eulerian–Lagrangian model (spray) outside the nozzle [23]. The goal is to improve the computational efficiency of the high-resolution simulations.

References

1 Medina M., Fatouraie M., Wooldridge M. (2018) High-speed imaging studies of gasoline fuel sprays at fuel injection pressures from 300 to 1500 bar, in: *WCX World Congress Experience*, SAE Technical Paper 2018-01-0294. https://doi.org/10.4271/2018-01-0294.

2 Koch D., Berger V., Bittel A., Gschwandtner M., Wachtmeister G., Chiodi M., Kaechele A., Bargende M., Wichelhaus D. (2019) Investigation of an innovative combustion process for high-performance engines and its impact on emissions, in: *International Powertrains, Fuels & Lubricants Meeting*, SAE Technical Paper 2019-01-0039. https://doi.org/10.4271/2019-01-0039.

3 Attard W., Bassett M., Parsons P., Blaxill B. (2011) A new combustion system achieving high drive cycle fuel economy improvements in a modern vehicle powertrain, in: *SAE 2011 World Congress & Exhibition*, SAE Technical Paper 2011-01-0664. https://doi.org/10.4271/2011-01-0664.

4 Kim C., Perry K., Viola M., Li W., Kushal N. (2011) Three-way catalyst design for urealess passive ammonia SCR: Lean-burn SIDI aftertreatment system, in: *SAE 2011 World Congress & Exhibition*, SAE Technical Paper 2011–01-0306. https://doi.org/10.4271/2011-01-0306.

5 Li S., Sarlioglu B., Jurkovic S., Patel N., Savagian P. (2016) Analysis of temperature effects on performance of interior permanent magnet machines, in: *2016 IEEE Energy Conversion Congress and Exposition (ECCE)*, September 18–22, Milwaukee Convention Center, Milwaukee, WI, USA, pp. 1–8. https://doi.org/10.1109/ECCE.2016.7855214.

6 Waclawczyk T., Koronowicz T. (2006) *Modeling of the wave breaking with CICSAM and HRIC High-resolution scheme*, ECCOMAS CFD, Egmond aan Zee, The Netherlands.

7 Wallscheid O., Huber T., Peters W., Böcker J. (2014) Real-time capable methods to determine the magnet temperature of permanent magnet synchronous motors – A review, in: *IECON 2014 – 40th Annual Conference of the IEEE Industrial Electronics Society*, 29 October – 01 November 2014, Dallas, TX, USA, pp. 811–818. https://doi.org/10.1109/IECON.2014.7048594.

8 Srinivasan C., Yang X., Schlautman J., Wang D., Srihari G. (2020) Conjugate heat transfer CFD analysis of an oil cooled automotive electrical motor, *SAE Int. J. Adv. Curr. Pract. Mobil.* **2**, 4, 1741–1753. https://doi.org/10.4271/2020-01-0168.

9 Wilcox D.C. (1988) *Turbulence modeling for CFD*, 2nd edn., DCW Industries, Inc.

10 Richards K.J., Senecal P.K., Pomraning E. (2017) *CONVERGE 2.4 Manual*, Convergent Science Inc., Madison, WI.

11 Senecal P.K., Pomraning E., Richards K.J., Briggs T.E., Choi C.Y., McDavid R.M., Patterson M.A., Hou S., Shethaji T. (2007) A new parallel cut-cell Cartesian CFD Code for rapid grid generation applied to in-cylinder diesel engine simulations, in: *SAE World Congress & Exhibition*, SAE Technical Paper #2007-01-0159.

12 Pomraning E., Richards K., Senecal P. (2014) Modeling turbulent combustion using a RANS model, detailed chemistry, and adaptive mesh refinement, in: *SAE 2014 World Congress & Exhibition*, SAE Technical Paper 2014-01-1116.

13 Waclawczyk T., Koronowicz T. (2006) *Modeling of the wave breaking with CICSAM and HRIC high-resolution scheme*, ECCOMAS CFD, Egmond aan Zee, The Netherlands.
14 Rhie C.M., Chow W.L. (1983) Numerical study of the turbulent flow past an airfoil with trailing edge separation, *AIAA J.* **21**, 1525–1532.
15 Menter F.R. (1994) Two-equation eddy-viscosity turbulence models for engineering applications, *AIAA J* **32**, 8, 269–289.
16 Lilly D.K. (1992) A proposed modification of the Germano Subgrid-Scale closure method, *Phys. Fluids A* **4**, 3, 633–635. https://doi.org/10.1063/1.858280.
17 Madabhushi R., Leong M., Arienti M., Brown C., McDonell V. (2006) On the breakup regime map of liquid jet in crossflow, in: *19th Annual Conference on Liquid Atomization and Spray Systems, May 2006*, 24–26 May, 2006, Toronto, CA.
18 Beck C., Schorr J., Echtle H., Verhagen J., Jooss A., Kruger C., Bargende M. (2021) Numerical and experimental investigation of flow phenomena in rotating step-holes for direct-spray-cooled electric motors, *Int. J. Engine Res.* **22**, 5, 1731–1740. https://doi.org/10.1177/1468087420918046.
19 Zhou Y., Williams R.J., Ramaprabhu P., Groom M., Thornber B., Hillier A., Mostert W., Rollin B., Balachandar S., Powell P.D., Mahalov A., Attal N. (2021) Rayleigh–Taylor and Richtmyer–Meshkov instabilities: a journey through scales, *Phys. D Nonlinear Phenom* **423**, 132838.
20 Sharp D.H. (1984) An overview of Rayleigh–Taylor instability, *Phys. D: Nonlinear Phenom.* **12**, 1–3, 3–10.
21 Zhou Y. (2017) Rayleigh–Taylor and Richtmyer–Meshkov instability induced flow, turbulence, and mixing II, *Phys. Rep.* **723**, 1–160.
22 Zhou Y. (2017) Rayleigh–Taylor and Richtmyer–Meshkov instability induced flow, turbulence, and mixing I, *Phys. Rep.* **720**, 1–136.
23 Beck C. (2020) *Numerische Analyse der Zweiphasenströmung und Kühlwirkung in nasslaufenden Elektromotoren*, Springer Fachmedien Wiesbaden GmbH.